Enhanced near-infrared photodetection with avalanche gain in silicon microdisk resonators integrated with *p-n* diodes

Haike Zhu, Linjie Zhou,* Rui Yang, Xinwan Li, and Jianping Chen

State Key Laboratory of Advanced Optical Communication Systems and Networks, Department of Electronic Engineering, Shanghai Jiao Tong University, Shanghai 200240, China

**Corresponding author: ljzhou@sjtu.edu.cn*

Received April 23, 2014; revised June 22, 2014; accepted June 22, 2014; posted June 24, 2014 (Doc. ID 210696); published July 29, 2014

We investigate the photocurrent generation by two-photon absorption effect in silicon microdisk resonators integrated with *p-n* diodes. The photocurrent is quite dependent on the *p-n* junction position with respect to the whispering gallery mode. Avalanche gain increases significantly when the bias exceeds −19 V, leading to considerable enhancement of photocurrent. At −22 V bias with on-chip optical power of 44.7 μW, the responsivity exceeds 1 A/W with an avalanche gain of 188 while the dark current is more than 50 times lower than the photocurrent. © 2014 Optical Society of America

OCIS codes: (130.0130) Integrated optics; (040.1345) Avalanche photodiodes (APDs); (230.5750) Resonators.
http://dx.doi.org/10.1364/OL.39.004525

Near-infrared (NIR) photodetection in all-silicon devices has opened up a new way to implement photodectectors and power monitors for integrated silicon photonics [1]. Compared to III-V or SiGe photodetectors, all-silicon photodetectors have a low responsivity at the telecom wavelength range due to the relatively large indirect bandgap. However, the major advantage of all-silicon photodetectors is that they are compatible with the complementary metal-oxide-semiconductor (CMOS) fabrication process, especially when we consider the potential low cost benefit of all-silicon photonic integrated systems [2,3]. The all-silicon photodetectors can be applicable only if the responsivity is comparable to that of III-V or Ge-Si devices. Using the midbandgap absorption (MBA) or internal photoemission absorption (IPA) mechanism does improve the responsivity of silicon photodetectors [4–6], but the Si^+ implantation and precise anneal temperature control [7] or the relatively complicated metal-silicon structure [8] makes the fabrication more complex and costly. Waveguide surface state absorption (SSA) can also be utilized for NIR photodetection, but its responsivity is rather weak due to the low absorption constant of surface states [9,10], making it only suitable for optical power monitors. Two photon absorption (TPA) is another mechanism that is promising for NIR photodetection, but the optical power needs to be high enough to initiate the nonlinear process to achieve a high responsivity [11,12].

Recently, we reported photocurrent generation in a microdisk resonator integrated with interleaved *p-n* junctions based on TPA [13]. In order to achieve a higher responsivity, current gain after photon absorption is needed [14]. The interleaved *p-n* junctions are more effective than the single *p-n* junction only if its interleaving period is small enough so that it has more junction field coverage over the optical mode. In this Letter, we demonstrate photocurrent generation based on the TPA effect in a microdisk resonator integrated with a single *p-n* junction. The *p-n* junction is positioned where the junction depletion region has a good coverage over the whispering gallery modes (WGMs) to make good use of the TPA effect. Increasing the reverse bias makes the internal electric field strong enough to initiate the avalanche effect. In this way, a high current gain is obtained. We fabricated two microdisks with different *p-n* junction locations. Our experiment results reveal that with optimal overlap between the WGM and the junction electric field, a considerably higher responsivity can be achieved than that in a silicon microring structure reported more recently [15], mainly due to the much stronger TPA effect in high-Q microdisks.

Figure 1(a) shows the schematic drawing of our device. The bus waveguide is 400 nm wide and 220 nm high with a slab thickness of 60 nm. The radius of the microdisk resonator is 6 μm. The gap between the waveguide and the microdisk is 250 nm. The doping concentration of the heavily doped p^+ and n^+ regions is $\sim 10^{20}$ cm^{-3} with a separation of $L_1 = 2.4$ μm. The lightly doped p and n regions have a doping concentration of $\sim 2 \times 10^{17}$ cm^{-3}. We designed two devices with different *p-n* junction positions in the disk. In device I the *p-n* junction has a separation of $L_2 = 0.6$ μm from the disk rim, and in device II the separation increases to 0.9 μm. The fabrication was done using the IME standard CMOS process [16]. Figure 1(b) shows the microscope image of the fabricated device.

Figure 2 shows the simulated junction electric field distribution and the three lowest radial order WGMs in

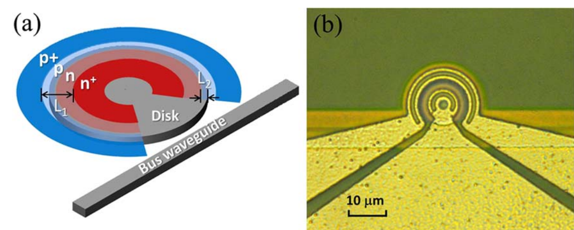

Fig. 1. (a) Schematic drawing of the *p-n* diode embedded microdisk resonator. (b) Microscope image of the fabricated device.

0146-9592/14/154525-04$15.00/0 © 2014 Optical Society of America

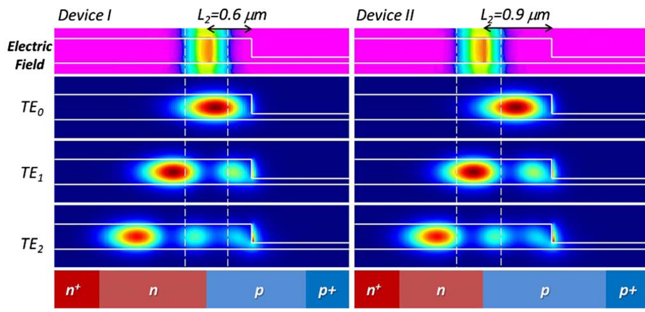

Fig. 2. Simulated electric field distribution in the *p-n* junction and three lowest radial order WGMs in devices I and II.

devices I and II. The *p-n* junction is biased at −22 V and its electric field is calculated by using the numerical simulation package from SILVACO. The maximum electric field in the center of the depletion region is over 7×10^5 V/cm. The edge of the depletion region is chosen where the electric field is 1×10^4 V/cm, below which the electric field is too weak to produce an effective multiplication [16]. Hence, the width of the depletion region is ~0.6 μm. The WGMs are calculated by solving the eigenfrequencies of the microdisk around 1.55 μm using the MODE solutions from Lumerical. Three transverse electric (TE) WGMs (TE_0, TE_1, and TE_2) are illustrated, where they have their intensity maxima around 0.5, 1, and 1.5 μm from the disk rim, respectively. In device I the junction electric field has a good coverage over the TE_0 mode, while in device II it has a good coverage over the TE_1 mode. Therefore, by comparing these two devices, we can study the influence of the *p-n* junction radial position on the current generation by various WGMs.

Figures 3(a) and 3(b) show the measured transmission spectra of devices I and II at a reverse bias of −3 V, respectively. The input power from the fiber is ~80.1 μW. The insertion loss (fiber to fiber) is ~18 dB, which is mainly caused by the coupling loss. The waveguide loss measured by the cutback method is around 3 dB/cm. Assuming the input and output coupling losses are equal, the estimated coupled optical power in the waveguide is ~10.2 μW. Input light is TE-polarized by using a polarization controller. An external DC voltage is applied onto the diode through a pair of metal probes. The resonance wavelengths (λ_0), *Q*-factors, and extinction ratios (ERs) for three resonance modes are listed in Table 1. We can see that TE_0 in both devices has the highest *Q*-factor, which is almost twice that of TE_1 and more than one order larger than that of TE_2. The increasing loss for higher-order WGMs is due to the free carrier absorption (FCA) by the inner n^+ doping region (see Fig. 2). The ERs of TE_0 and TE_1 in both devices are over 10 dB, indicating a good balance between the cavity loss and the coupling strength. Given their higher *Q*-factors and ERs, these two modes have more optical energy stored in the microdisk than that of TE_2.

Figures 3(c) and 3(d) show the measured current as a function of wavelength for devices I and II, respectively. The collected current is recorded by an I/V measuring unit (Agilent B2912A) while the wavelength is scanning. The measurements were performed at room temperature, and the current was recorded under thermal balance. As the bias voltage is only −3 V, the avalanche

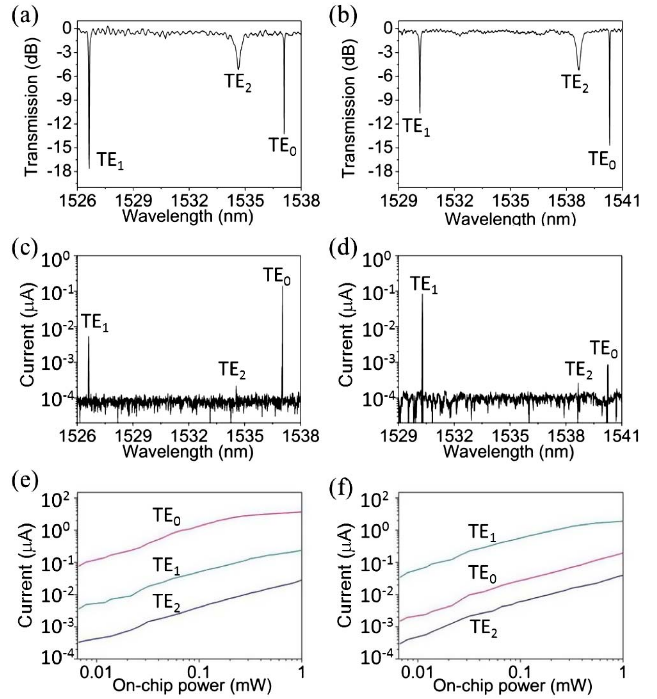

Fig. 3. (a) and (b) Measured transmission spectra showing three resonance modes (TE_0, TE_1, and TE_2). (c) and (d) Measured current spectra. (e) and (f) Measured peak current as a function of on-chip optical power. The bias voltage is −3 V. The left column of plots is for device I and the right for device II.

effect is negligible. Therefore, we can characterize the photon absorption from these three WGMs without concerning ourselves with the multiplication effect. In device I, TE_0 generates the highest current of more than 0.1 μA, which is over one order higher than that of TE_1 and over two orders higher than that of TE_2. As TE_2 has a weak interaction with the junction electric field together with its low Q-factor and ER, the current generated by TE_2 is only slightly higher than the background. In device II, however, TE_1 generates the highest current of ~0.1 μA, which is over one order higher than that of TE_0 and over two orders higher than TE_2. It hence reveals that the position of *p-n* junction plays a significant role in current generation by a particular WGM.

Figures 3(e) and 3(f) show the current generated by the three WGMs as a function of on-chip power at −3 V. The input light is fixed at the resonance wavelength of each WGM and amplified by an erbium-doped optical fiber amplifier (EDFA) to boost the optical power,

Table 1. Resonance Properties of the Microdisk WGMs

	TE_0	TE_1	TE_2
	Device I		
λ_0 (nm)	1537.1	1526.6	1534.5
Q-factor	6.1×10^4	2.6×10^4	3.7×10^3
ER (dB)	13	18	5
	Device II		
λ_0 (nm)	1540.2	1530.2	1538.7
Q-factor	5.2×10^4	2.9×10^4	3.6×10^3
ER (dB)	15	11	5

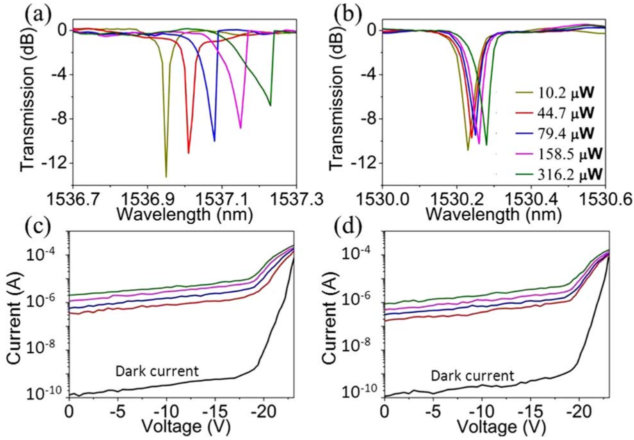

Fig. 4. (a) and (b) Measured transmission spectra under various on-chip power levels at −3 V. (c) and (d) Measured peak current as a function of reverse bias. The left column of plots is for TE_0 in device I and the right for TE_1 in device II.

followed by a 1-nm bandwidth optical filter to suppress the amplified spontaneous emission (ASE) noise. The input power is adjustable by tuning the EDFA gain. The generated current from the WGMs all rises quickly with increasing optical power. However, at high optical power, the increment of current for TE_0 in device I and TE_1 in device II gradually slows down, indicating FCA induced by the strong TPA taking effect [12].

We select TE_0 in device I and TE_1 in device II to further study their performance in photodetection. Figures 4(a) and 4(b) show the measured transmission spectra under various on-chip optical power levels at −3 V. As the optical power increases, the resonance gradually red-shifts with an asymmetric resonance line shape, indicating the thermo-optic (TO) effect following FCA is very strong. TE_0 in device I has a larger red-shift than that of TE_1 in device II under the same optical power level, suggesting a stronger TPA effect for TE_0 in device I. In fact, by fitting the transmission spectra with a theoretical model [17], we can derive the optical power resonance enhancement factor of 605 and 455 for TE_0 in device I and TE_1 in device II, respectively. Therefore, the optical power of TE_0 in device I is higher than that of TE_1 in device II under the same on-chip waveguide power. Another factor that may also result in a larger red-shift of TE_0 is that TE_0 has a smaller mode effective area since TE_0 has only one mode peak while TE_1 has two peaks with its power less concentrated.

Figures 4(c) and 4(d) show the measured current as a function of reverse bias. The dark current in both devices slowly increases with the reverse bias before −19 V. After −19 V, the dark current shows a rapid increase where a very strong avalanche effect takes place. It reaches ~70 μA at −23 V, which is more than five orders larger than the dark current at 0 V. In Fig. 4(c), with 44.7 μW on-chip power in device I, the current is $\sim 4 \times 10^{-7}$ A at 0 V and $\sim 1.4 \times 10^{-4}$ A at −23 V, an increase of 350 times. The voltage sensitivity of the current is $\sim 6.3 \times 10^{-5}$ A/V at −22 V. It reduces with the increasing on-chip power. Figure 4(d) shows almost the same current increment trend with reverse bias except that the current is ~2 times lower than that in Fig. 4(c) before −19 V due to the weaker TPA effect. The current increases 387 times at −23 V than that at 0 V with 44.7 μW on-chip optical power. The voltage sensitivity of the current is $\sim 7.9 \times 10^{-5}$ A/V at −22 V. After −23 V, the current becomes unstable and insensitive to bias voltage because of the increased multiplication noise and space charge effect [18].

We define a parameter κ as the ratio between the photocurrent and the dark current that reflects the signal-to-noise ratio. The photocurrent is obtained by subtracting the dark current from the measured current under illumination. Figure 5(a) shows κ curves for TE_0 in device I extracted from Fig. 4(c). It can be seen that κ is very high (over 1000) for the power levels in our experiment before −19 V. However, it falls rapidly with the reverse bias after −19 V, where the avalanche effect is strong. Figure 5(b) shows the κ curves for TE_1 in device II. κ is a little lower than the former one at the same power level and bias. In both devices, κ drops close to 1 when the bias approaches −23 V. Figures 5(c) and 5(d) show the responsivity R and avalanche gain M in the two devices. The responsivity shown in Figs. 4(c) and 4(d) was the result of using 44.7 μW on-chip power. We

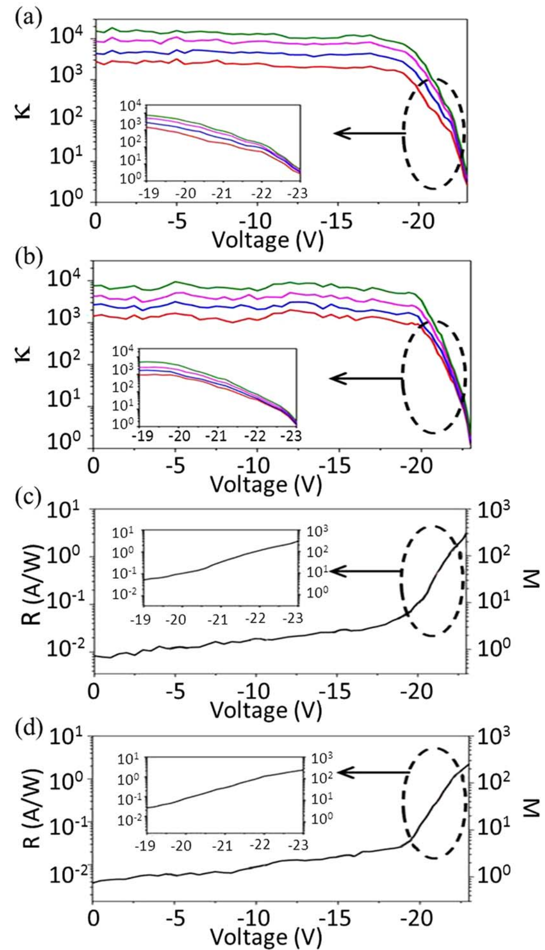

Fig. 5. (a) and (b) Contrast ratio between the photocurrent and the dark current at various on-chip power levels as a function of reverse bias. (c) and (d) Responsivity and avalanche gain as a function of reverse bias. (a) and (c): TE_0 in device I; (b) and (d): TE_1 in device II. Insets: magnified plots for the voltage range from −19 V to −23 V.

can see that both responsivities are below 0.01 A/W at 0 V but rise quickly with reverse bias, especially from −19 V to −23 V. The responsivities exceed 1 A/W at −22 V. The avalanche gain is defined as the magnification of photocurrent with respect to that at −5 V, where the depletion width is almost stable. In order to find the avalanche breakdown voltage of our devices, we use the Miller formula [19]

$$M = [1 - (V/V_b)^n]^{-1},$$

where V is the applied voltage, V_b is the avalanche breakdown voltage, and n is a constant that is 1.5–4 for silicon. After fitting the experimental data, we get $V_b = -22.4$ V and $n = 1.6$.

The insets in Fig. 5 show the magnified plots of κ and responsivity curves from −19 V to −23 V. The voltage sensitivities of responsivity are ~1.4 and ~1.7 $\mathrm{A/(W \cdot V)}$ at −22 V for devices I and II, respectively. One can see that a higher responsivity is obtained at the cost of a smaller κ, suggesting a trade-off behavior between them. For example, with 44.7 μW power and at −22 V bias, the responsivity reaches 1.15 A/W (avalanche gain of 188) for TE_0 of device I, but κ is only 53. At −20 V bias, although the responsivity is reduced to ~0.1 A/W (avalanche gain 10), κ rises to 466. We attribute the high κ to the strong TPA effect in the high-Q microdisk resonator. The relatively low doping concentration ensures the high Q-factor of the resonances that favors the photon energy buildup in the resonator. It also provides a large depletion area for photon absorption, yet a high reverse bias is needed to generate a strong avalanche effect.

In summary, we investigated the photocurrent generation by TPA effect in microdisk resonators embedded with *p-n* diodes. The location of the *p-n* junction with respect to the WGM plays a significant role in photocurrent generation. To obtain a high photocurrent, the *p-n* junction needs to overlap sufficiently with the intensity peak of the WGMs. Our measurement reveals that significant avalanche effect takes place after −19 V where the photocurrent sees a rapid increase with revere bias. The enhanced responsivity by the avalanche effect is compromised by the increased dark current. With 44.7 μW on-chip power and near the breakdown voltage of ~22 V, the responsivity can be as large as 1 A/W while the photocurrent is still more than 50 times larger than the dark current. κ could be further increased either by using a higher Q-factor microdisk to further enhance the TPA effect, or by lowering the doping concentration to widen the depletion region for more photon absorption at the cost of a higher breakdown voltage. This kind of device can not only be used as a wavelength-selective photodetector, it can also be used to selectively monitor a certain WGM by properly positioning the *p-n* junction.

This work was supported in part by the 973 program (ID2011CB301700), the 863 program (2013AA014402), the National Natural Science Foundation of China (NSFC) (61127016, 61107041), the Science and Technology Commission of Shanghai Municipality (STCSM) Project (12XD1406400). We also acknowledge IME Singapore for device fabrication.

References

1. M. Casalino, G. Coppola, M. Iodice, I. Rendina, and L. Sirleto, Sensors **10**, 10571 (2010).
2. B. Jalali and S. Fathpour, J. Lightwave Technol. **24**, 4600 (2006).
3. N. Izhaky, M. T. Morse, S. Koehl, O. Cohen, D. Rubin, A. Barkai, G. Sarid, R. Cohen, and M. J. Paniccia, IEEE J. Selec. Topics Quantum Electron. **12**, 1688 (2006).
4. M. W. Geis, S. J. Spector, M. E. Grein, R. T. Schulein, J. U. Yoon, D. M. Lennon, S. Deneault, F. Gan, F. X. Kaertner, and T. M. Lyszczarz, IEEE Photon. Technol. Lett. **19**, 152 (2007).
5. D. F. Logan, P. Velha, M. Sorel, R. M. De La Rue, A. P. Knights, and P. E. Jessop, IEEE Photon. Technol. Lett. **22**, 1530 (2010).
6. S. Zhu, G. Q. Lo, M. B. Yu, and D. L. Kwong, Appl. Phys. Lett. **93**, 071108 (2008).
7. D. F. Logan, P. Velha, M. Sorel, R. M. De La Rue, P. E. Jessop, and A. P. Knights, IEEE Photon. Technol. Lett. **24**, 261 (2012).
8. M. Casalino, L. Sirleto, L. Moretti, and I. Rendina, Semicond. Sci. Technol. **23**, 075001 (2008).
9. H. Chen, X. Luo, and A. W. Poon, Appl. Phys. Lett. **95**, 171111 (2009).
10. T. Baehr-Jones, M. Hochberg, and A. Scherer, Opt. Express **16**, 1659 (2008).
11. H. Chen and A. W. Poon, Appl. Phys. Lett. **96**, 191106 (2010).
12. T. Tanabe, H. Sumikura, H. Taniyama, A. Shinya, and M. Notomi, Appl. Phys. Lett. **96**, 101103 (2010).
13. H. Zhu, L. Zhou, X. Sun, J. Xie, X. Li, and J. Chen, in *Conference on Lasers and Electro-optics: Science and Innovations*, OSA Technical Digest (Optical Society of America, 2013), paper JTh2A.38.
14. Y. Zhao, C. Xu, X. Jiang, and H. Ge, J. Semicond. **34**, 064009 (2013).
15. Y. Li, S. Feng, Y. Zhang, and A. W. Poon, Opt. Lett. **38**, 5200 (2013).
16. L. Tsung-Yang, A. Kah-Wee, F. Qing, S. Jun-Feng, X. Yong-Zhong, Y. Ming-Bin, L. Guo-Qiang, and K. Dim-Lee, J. Sel. Top. Quantum Electron., **16**, 307 (2010).
17. L. Vivien and L. Pavesi, in *Handbook of Silicon Photonics* (Taylor & Francis, 2013), pp. 155–168.
18. S. M. Sze and K. K. Ng, in *Physics of Semiconductor Devices* (Wiley, 2014), pp. 49–50.
19. S. Miller, Phys. Rev. **99**, 1234 (1955).